Unified Flux Control Architecture for Fluxonium Qubits

Xianchuang Pan,[1,*] Jiahui Wang,[1,*] Tao Zhou,[1,*] Yanbo Guo,[1] Fei Wang,[1] Ze Zhan,[1] Liang Xiang,[1] Zishuo Li,[1] Lu Ma,[1] Xizheng Ma,[1] Huijuan Zhan,[1] Tao Zhang,[1] Kannan Lu,[1] Xing Zhu,[1,†] Guicheng Gong,[1] Chunqing Deng,[1,‡] and Tenghui Wang[1,§]

[1]*S Lab, Quantum Science Center of Guangdong-Hong Kong-Macao Greater Bay Area, Shenzhen, China*

(Dated: June 1, 2026)

Control architectures that reduce hardware overhead while maintaining high-fidelity operations are essential for the continued scaling of superconducting quantum processors. Here we experimentally realize a unified control architecture for fluxonium qubits, in which both transverse (XY) and longitudinal (Z) operations are implemented through a single flux-control channel driven by a single arbitrary waveform generator channel. This architecture imposes competing requirements on the shared control channel, which must simultaneously support low-frequency flux transmission for reset operations while strongly attenuating broadband noise near the qubit transition frequency. We address this challenge through frequency-selective cryogenic filtering together with compensated waveform synthesis that corrects the pulse distortion introduced by the filtered control line. Experimentally, this approach preserves coherence times above 100 μs while enabling active reset with approximately 98% fidelity and 20-ns single-qubit gates with fidelities exceeding 99.99%. We further demonstrate FPGA-native instruction-level waveform synthesis based on reusable pulse primitives for unified flux control. These results establish unified flux control as a scalable architecture for fluxonium qubits that reduces control hardware overhead while preserving high-fidelity operation.

I. INTRODUCTION

Superconducting quantum circuits are among the leading platforms for quantum information processing, with rapid advances in coherence [1–5], gate fidelity [6–10], and processor scale [11–15]. As these systems continue to scale, however, the complexity of the control architecture itself increasingly becomes a limiting factor. In most superconducting platforms, universal qubit control relies on multiple physically distinct channels: transverse (XY) operations are implemented using microwave charge drive, while longitudinal (Z) control is realized through low-frequency flux bias [16–18]. This separation requires duplicated electronic sources, filtering stages, and calibration abstractions. Several approaches have attempted to reduce wiring complexity by integrating microwave and flux pathways within a shared on-chip structure [19, 20]. However, these approaches still rely on multiple independent control sources operating across different spectral regimes. As a result, the underlying control paradigm remains fundamentally multi-channel, inherently limiting further architectural simplification.

Unlike superconducting qubits based on plasmon-like excitations in circuits such as the transmon, flux-like qubits such as fluxonium derive their qubit transitions from fluxon tunneling. In these systems, both transverse and longitudinal control can be implemented through the same inductive flux degree of freedom [9, 21–23]. Accordingly, transverse rotations are driven by modulated ac flux signals, while longitudinal operations are implemented through quasi-dc flux bias. Ultimately, universal single-qubit control can be collapsed into a single inductive channel. This unified control channel enables architectural simplification while remaining compatible with the operating regime in which fluxonium qubits have demonstrated long coherence times [3–5] and high-fidelity gate performance [8–10, 21, 23–27].

However, consolidating universal control into a shared physical channel introduces nontrivial engineering challenges. The same line must simultaneously preserve strong low-frequency transmission for large flux excursions and active reset [27–29], while strongly attenuating broadband noise near the qubit transition frequency to protect coherence [30, 31]. In practice, the required line response is difficult to realize: the channel must be nearly transparent near dc while providing spectrally flat attenuation around the qubit transition frequency (hundreds of MHz). Residual amplitude/phase ripple then distorts the microwave flux modulation and degrades XY-control fidelity. Approaches exploiting higher-order nonlinear processes have recently been explored to partially relax this filtering constraint by enabling control at subharmonic frequencies through filtered lines [32, 33]. However, these schemes generally require higher-order nonlinear processes and introduce additional calibration complexity, including amplitude-dependent frequency shifts and reduced effective coupling strengths.

In this work, we experimentally realize a unified control architecture for fluxonium qubits through a joint design of cryogenic filtering and compensated waveform synthesis. We first show that frequency-selective cryogenic filtering preserves long coherence while maintaining the flux tuning range required for flux-controlled reset. We then introduce a bounded inverse-filtering framework that compensates waveform distortion, enabling high-

* These authors contributed equally to this work.
† zhuxing@quantumsc.cn
‡ dengchunqing@quantumsc.cn
§ wangtenghui@quantumsc.cn

contrast Rabi oscillations, active reset, and single-qubit gate fidelities above 99.99% within a unified flux control channel. Building on this calibrated control layer, we further implement FPGA-native instruction-level waveform synthesis based on reusable pulse primitives, enabling complex control sequences to be dynamically generated within the same unified control framework. Together, these results establish flux control as a unified architecture for fluxonium qubits.

II. UNIFIED FLUX CONTROL ARCHITECTURE

In this section, we present the unified control architecture for the fluxonium qubit. As depicted in Fig. 1(a), unlike conventional architectures that require separate charge and flux lines, our design utilizes a single unified flux line to mediate all necessary control signals. The system is governed by the fluxonium Hamiltonian,

$$H_0 = 4E_C\hat{n}^2 + \frac{1}{2}E_L(\hat{\phi} - \phi_{\text{ext}})^2 - E_J\cos(\hat{\phi}), \quad (1)$$

where E_C, E_L, and E_J are the charging, inductive, and Josephson energies, respectively, and $\phi_{\text{ext}} = 2\pi\Phi_{\text{ext}}/\Phi_0$ is the reduced external magnetic flux. The control signals are synthesized by an arbitrary waveform generator (AWG) at room temperature, attenuated by a total factor of α inside the dilution refrigerator, and inductively coupled to the qubit through a mutual inductance M. Consequently, the total external flux can be decomposed into a static bias and time-dependent control components,

$$\Phi_{\text{ext}}(t) = \Phi_{\text{dc}} + \delta\Phi_{\text{dc}}(t) + \Phi_{\text{ac}}(t). \quad (2)$$

Fig. 1(b) illustrates the fluxonium spectrum together with the corresponding unified control protocol. The qubit is typically biased at the half-flux sweet spot ($\Phi_{\text{dc}} = 0.5\Phi_0$), where first-order sensitivity to flux noise vanishes. At this operating point, the $|g\rangle \to |e\rangle$ transition frequency is strongly suppressed and typically lies in the 200–400 MHz range. As indicated by the dashed arrows in Fig. 1(b), the shared flux-control line simultaneously supports universal control by applying both a microwave component $\Phi_{\text{ac}}(t)$ for resonant XY rotations and a baseband component $\delta\Phi_{\text{dc}}(t)$ for dynamically shifting the qubit to higher frequencies during initialization. When the readout cavity frequency is designed below the maximum qubit transition frequency, dynamic flux tuning can further bring the qubit close to resonance with the cavity, enhancing qubit–cavity interaction and enabling accelerated reset. In this way, universal single-qubit control is implemented within a single flux control framework.

For the spectrum shown in Fig. 1(b), we adopt device parameters of $E_J/h = 4.5$ GHz, $E_C/h = 1.1$ GHz, and $E_L/h = 0.5$ GHz, together with a readout resonator frequency $f_r = 4.98$ GHz. These values are consistent with experimentally realized fluxonium devices and reflect typical operating conditions in our setup. However, implementing universal control through a shared flux-control line introduces an intrinsic bandwidth-distortion tradeoff. From the linear expansion of the inductive energy [34], the effective Rabi drive strength Ω_R is directly proportional to the total line transmission factor α:

$$\hbar\Omega_R = \left|2\pi E_L \frac{M}{\Phi_0}\frac{\alpha}{Z_0}\right| V_0 |\langle 0|\hat{\phi}|1\rangle|, \quad (3)$$

where V_0 is the room-temperature drive amplitude and Z_0 is the line impedance. At the same time, wideband noise from room-temperature electronics propagates through the same control line and induces qubit relaxation through environmental voltage fluctuations [35]. Within a Fermi's Golden Rule treatment, the corresponding relaxation rate $\Gamma_{1\to 0}^{\text{line}} = 1/T_1^{\text{line}}$ scales quadratically with the line transmission factor α,

$$\frac{1}{T_1^{\text{line}}} = \frac{1}{\hbar^2}\left(2\pi E_L \frac{M}{\Phi_0}\frac{\alpha}{Z_0}\right)^2 |\langle 0|\hat{\phi}|1\rangle|^2 S_{VV}^{\text{awg}}(\omega_{ge}), \quad (4)$$

where $S_{VV}^{\text{awg}}(\omega_{ge})$ denotes the effective voltage-noise spectral density at the AWG output. The detailed calculation is summarized in Appendix A.

To quantify this tradeoff, we assume a mutual inductance of $M = 2$ pH and a typical commercial AWG with active wideband noise characterized by a power spectral density of -130 dBm/Hz. Fixing the maximum AWG output amplitude at $V_0 = 0.5$ V, we evaluate the resulting coherence limit together with the achievable controllability for gate operations and initialization across different attenuation factors. The resulting tradeoff defines a central constraint of the unified architecture, as summarized in Fig. 1(c). In the high-coherence regime (heavy attenuation, $\alpha \approx -80$ to -50 dB), the qubit maintains coherence times exceeding 10^2 μs, but only weak drive amplitudes reach the device, resulting in slow gate operations. Conversely, in the strong-reset regime (light attenuation, $\alpha \approx -30$ to -20 dB with maximum $\delta\Phi_{\text{dc}}/\Phi_0 \geq 0.3$), large flux excursions become accessible for rapid modulation and reset, but coherence is strongly degraded by broadband noise injection. These results highlight that realizing this unified architecture requires careful engineering of the attenuation chain, strictly necessitating the deployment of frequency-selective filtering to suppress $S_{VV}^{\text{awg}}(\omega_{ge})$ while maintaining high signal transparency at baseband frequencies.

III. EXPERIMENTAL DEMONSTRATION OF UNIFIED FLUX CONTROL

We now implement unified flux control using frequency-selective filtering to resolve the coherence-versus-control trade-off identified in the previous section. The detailed cryogenic setup is provided in Appendix B.

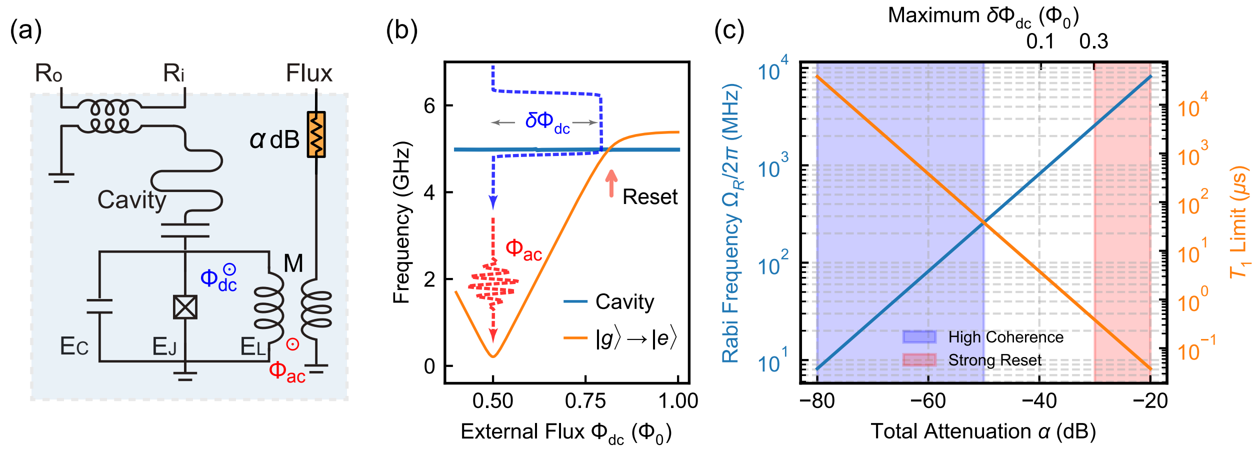

FIG. 1. **Unified Flux Control Architecture**. (a) Circuit schematic of a fluxonium qubit coupled to a single unified flux line. The control signals undergo a total attenuation of α before coupling to the qubit via a mutual inductance M. (b) Energy spectrum of the fluxonium and the readout cavity as a function of the external static flux $\Phi_{\rm dc}$. The dashed arrows illustrate the multiplexed control protocol at the half-flux sweet spot ($\Phi_{\rm dc} = 0.5\Phi_0$): a microwave pulse $\Phi_{\rm ac}$ drives the transverse $|g\rangle \to |e\rangle$ transition for single-qubit gates, while a baseband pulse $\delta\Phi_{\rm dc}$ longitudinally tunes the qubit frequency toward the cavity for rapid initialization. (c) Calculated Rabi frequency $\Omega_R/2\pi$ (blue, left axis) and the T_1 relaxation limit induced by room-temperature wideband noise (orange, right axis) versus the total line attenuation α. The top axis indicates the corresponding maximum achievable DC flux excursion. The shaded areas denote the "High Coherence" regime (blue) and the "Strong Reset" regime (red), illustrating the strict necessity for frequency-selective filtering in the single-port design.

For a fluxonium qubit with transition frequency f_q = 208 MHz, the control line incorporates a Gaussian low-pass filter with a 3-dB cutoff frequency of $f_c \approx 92$ MHz and transfer function $H_{\rm gauss}(f) = \exp[-(f\sigma)^2/2]$, providing approximately 18 dB attenuation at the qubit frequency. Combined with the 30 dB cryogenic attenuation and cable losses, the total attenuation exceeds 50 dB, strongly suppressing broadband noise from room-temperature electronics. Under these conditions, the qubit remains within the high-coherence regime, with measured coherence times of $T_1 = 110$ μs, $T_2^{\rm R} = 128$ μs, and $T_2^{\rm echo} = 133$ μs. A detailed coherence analysis is provided in Appendix C.

The same filtering, however, inevitably distorts short control pulses because of its finite bandwidth and associated phase dispersion. To compensate for this effect, we apply a pre-distortion procedure that reshapes the input waveform such that the combined response of the control line is approximately flat over the qubit operation band. Instead of implementing a direct reciprocal filter, which would diverge at high frequencies, we construct a bounded inverse filter that selectively compensates attenuation near the qubit frequency while remaining stable elsewhere. The inverse filter is defined as

$$H_{\rm inv}(f) = \frac{H_{\rm qubit}}{\max[H_{\rm gauss}(f), 10^{-G_{\rm max}/20}]} \times W(f), \qquad (5)$$

where $H_{\rm qubit} = H_{\rm gauss}(f_q)$ sets the normalization at the qubit frequency. The maximum gain is capped at $G_{\rm max}$ = 50 dB to avoid numerical divergence and AWG saturation, while the Gaussian window $W(f) = \exp[-(f\sigma_w)^2/2]$ suppresses compensation outside the target bandwidth with a 3-dB cutoff near 1 GHz.

The resulting compensation procedure is illustrated in Fig. 2(a). The upper panel compares the bounded inverse filter $H_{\rm inv}(f)$ (blue), the Gaussian line response $H_{\rm gauss}(f)$ (orange), and the resulting effective transfer function $H_{\rm prod}(f) = H_{\rm gauss}(f)H_{\rm inv}(f)$ (green). The compensated response remains approximately flat around f_q while preserving strong attenuation outside the operational band. In the time domain, shown in the lower panel of Fig. 2(a), the pre-distorted waveform generated by the AWG contains additional high-frequency components that counteract the filtering-induced distortion, thereby recovering the intended pulse shape at the qubit. We first implement this compensation entirely in software, without additional hardware modifications.

The necessity and effectiveness of the pre-distortion procedure are verified experimentally through the Rabi measurements shown in Fig. 2(b). Without pre-distortion, the oscillations exhibit strongly reduced contrast and fail to achieve complete population inversion, particularly for short pulses with broad spectral content. With pre-distortion enabled, high-contrast sinusoidal Rabi oscillations are recovered, confirming that accurate single-port control can be maintained despite the strong low-pass filtering. We next demonstrate the active-reset protocol enabled within the same unified control framework. Following the operating principle illustrated in Fig. 1(b), a quasi-dc flux excursion of $\Delta\Phi_{\rm dc} \approx 0.298\Phi_0$ is applied to bring the qubit close to resonance with the readout cavity, where it remains for approximately 5 μs to enhance energy relaxation. Fig. 2(c) shows the rotated readout histograms together with Gaussian

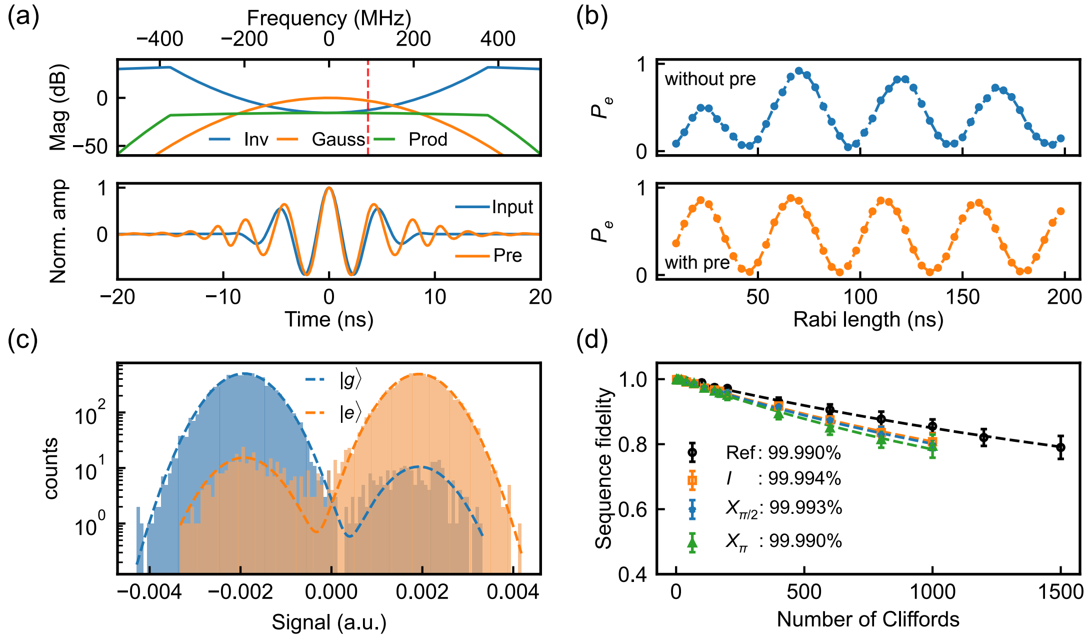

FIG. 2. **Experimental Demonstration of Unified Flux Control.** (a) Frequency- and time-domain illustration of the pre-distortion procedure. Top: the bounded inverse filter $H_{\text{inv}}(f)$ (blue), the Gaussian low-pass transfer function $H_{\text{gauss}}(f)$ (orange), and the resulting effective response $H_{\text{prod}}(f) = H_{\text{gauss}}(f)H_{\text{inv}}(f)$ (green). Bottom: comparison between the target input waveform (blue) and the pre-distorted waveform generated by the AWG (orange). (b) Rabi oscillations measured without pre-distortion (top, blue) and with pre-distortion (bottom, orange). Pre-distortion restores high-contrast oscillations and enables nearly complete population transfer. (c) Histograms of the rotated readout signal together with Gaussian fits for the $|g\rangle$ (blue) and $|e\rangle$ (orange) state references, used to estimate the residual excited-state population after the reset protocol. (d) Standard randomized benchmarking and interleaved randomized benchmarking for 20-ns single-qubit gates. Black circles: reference RB; orange squares: interleaved I gate; blue diamonds: interleaved $X_{\pi/2}$ gate; green triangles: interleaved X_π gate. The extracted gate fidelities are all at or above 99.99%.

fits for the $|g\rangle$ (blue) and $|e\rangle$ (orange) state references [25]. From the overlap analysis, we extract a residual excited-state population of approximately 2%, corresponding to an initialization fidelity near 98%. Although the present protocol is not optimized for speed, substantially faster initialization should be achievable with optimized flux trajectories and device parameters.

Finally, we benchmark single-qubit gate performance within the unified flux-control architecture. We employ standard cosine pulse envelopes and follow a calibration protocol identical to that described in Ref. [25]. Using a gate duration of 20 ns, we perform standard randomized benchmarking (RB) together with interleaved randomized benchmarking (iRB) [36], as shown in Fig. 2(d). The black circles denote the reference RB sequence, while the orange squares, blue diamonds, and green triangles correspond to interleaved benchmarking of the I, $X_{\pi/2}$, and X_π gates, respectively. The extracted fidelities for these representative single-qubit gates are all at or above 99.99%. Furthermore, as detailed in the Appendix D, we have systematically benchmarked multiple qubits across various operating frequencies, all of which consistently exhibit fidelities at the 99.99% level. These comprehensive results demonstrate that high-fidelity quantum operations can be robustly achieved across different device parameters within the unified single-port architecture.

IV. INSTRUCTION-LEVEL WAVEFORM SYNTHESIS FOR UNIFIED FLUX CONTROL

While software-level pre-distortion establishes the feasibility of unified flux control, scalability ultimately requires elevating waveform generation from stored data to dynamic synthesis. Precomputing and storing fully distorted waveforms is intrinsically non-scalable, as it ties control complexity directly to memory resources and limits runtime flexibility. A more general approach is to treat control waveforms as compositions of reusable waveform primitives, generated and conditioned during execution.

Guided by this principle, we implement an FPGA-based control architecture in which the AWG operates as an instruction-driven waveform synthesizer, as shown in Fig. 3(a). Instead of uploading explicit waveforms, the host provides a compact sequence of operations that reference a minimal set of reusable waveform primitives together with timing and frequency parameters [37]. Representative primitives, including baseband flux edges and

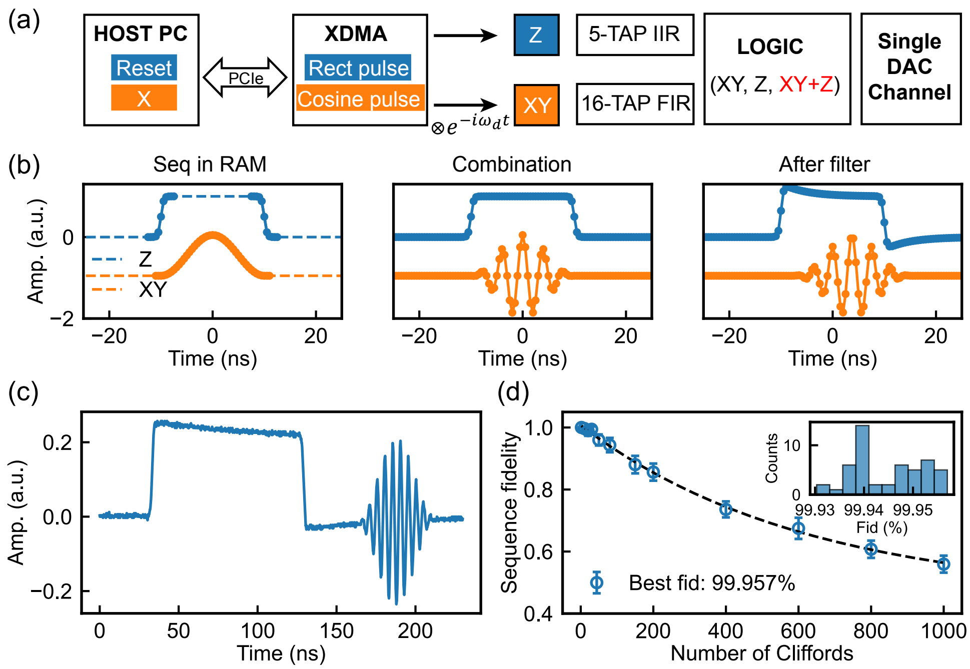

FIG. 3. **Instruction-level Waveform Synthesis for Unified Flux Control.** (a) Control architecture. A host PC sends instruction sequences via PCIe to the AWG, where waveform primitives are stored in onboard memory. The FPGA performs real-time modulation of the XY envelope at frequency ω_d, applies digital filtering to the Z and XY paths (5-tap IIR and 16-tap FIR, respectively), and routes the resulting composite $(XY+Z)$ waveform to a single DAC channel. (b) Waveform synthesis process. Left: stored primitives, including baseband flux edges and a resonant cosine envelope. Middle: assembled and modulated waveforms prior to filtering. Right: output waveforms after digital compensation. (c) Measured AWG output for a composite $(XY+Z)$ waveform. (d) Randomized benchmarking of a fluxonium qubit using this control scheme. The extracted single-qubit gate fidelity is 99.957%. Inset: distribution over repeated runs.

resonant cosine envelopes, are shown in the left panel of Fig. 3(b). During execution, the FPGA dynamically assembles and modulates these segments to synthesize the target control signals, as illustrated in the middle panel of Fig. 3(b). In particular,the resonant envelope is modulated by a carrier $e^{-i\omega_d t}$ matched to the selected qubit, thus decoupling logical operations from their physical waveform representations. Within this framework, compensation of control-line distortions is incorporated directly into the synthesis process. The Z and XY paths are conditioned independently through embedded digital filters: a 5-tap infinite impulse response (IIR) filter suppresses long-timescale distortions associated with slow flux-line dynamics, while a 16-tap finite impulse response (FIR) filter performs dynamic predistortion of the microwave-modulated component [38]. Detailed characterization of these channel distortions is provided in the Appendix E. The conditioned baseband and microwave-modulated components are then summed and emitted as a single composite waveform $(XY+Z)$ through one digital-to-analog converter (DAC). The resulting filtered waveforms are shown in the right panel of Fig. 3(b). In this way, control is implemented through dynamic signal synthesis rather than stored waveform replay.

Experimentally, the synthesized output waveform, including simultaneous baseband and microwave-modulated components (i.e., $XY+Z$), closely matches the designed structure [Fig. 3(c)], with the specific FIR coefficients detailed in Appendix F. To further validate the generality of this approach, we benchmark single-qubit gates on a separate fluxonium qubit operated at 202 MHz in a different cooldown, with measured coherence times of $T_1 \sim 40\,\mu$s and $T_2^{\mathrm{R}} \sim 13\,\mu$s and a gate duration of 28 ns. Randomized benchmarking yields a best gate fidelity of 99.957% [Fig. 3(d)], approaching the coherence limit.

Notably, long gate sequences are synthesized dynamically from short primitive segments: in our implementation, sequences exceeding 50 μs in duration require storing less than 100 ns of waveform data. This abstraction leads to a substantial reduction in memory requirements. Rather than storing fully synthesized analog waveforms for every operation, the complete set of single-qubit controls can be generated from only a small library of reusable primitives. Higher-level operations, such as virtual-Z phase updates, are resolved directly at the instruction level without additional waveform storage. Consequently, the program description (number of instructions and associated parameters) scales with the instruction set rather than with the stored waveform volume, enabling efficient and flexible programmability.

Critically, the entire synthesized control stream is delivered through a single DAC channel, providing a direct hardware-level reduction in per-qubit control overhead.

V. CONCLUSION AND OUTLOOK

We have introduced and experimentally validated a unified flux control architecture for fluxonium qubits. The central challenge of this architecture is to reconcile three competing requirements within a single physical control channel: suppression of room-temperature wideband noise to preserve coherence, sufficient low-frequency transmission for large flux excursions and active reset, and accurate microwave delivery for high-fidelity gate operations. Our results show that these competing requirements can be resolved through the joint design of frequency-selective filtering and compensated waveform synthesis.

Specifically, frequency-selective filtering enables operation in the high-coherence regime while preserving the low-frequency control range required for initialization, and compensated pulse synthesis corrects the distortion of short microwave pulses introduced by the line response. Furthermore, to reduce electronics overhead, we implement instruction-based waveform generation on FPGA, where a compact set of reusable waveform primitives replaces stored waveform replay. Together, these elements establish a unified control framework that reduces wiring and electronics overhead while preserving coherence and enabling high-fidelity control.

This reduction in control hardware is a direct consequence of a fluxonium-specific feature: owing to its transition frequency in the hundreds-of-megahertz range, the microwave-modulated component for resonant driving and the baseband component for flux tuning can be synthesized and delivered as a single composite ($XY+Z$) waveform from one AWG/DAC channel per qubit with only moderate bandwidth requirements. By contrast, the few-gigahertz transition frequency of the transmon imposes a much larger bandwidth requirement, typically forcing the use of separate channels for low-bandwidth Z control and high-bandwidth microwave XY drive, combined only at room temperature. This makes the transmon control stack intrinsically more hardware-intensive, whereas fluxonium allows a substantially smaller room-temperature electronics footprint per qubit.

More broadly, this work identifies a general design principle for unified flux control: passive spectral shaping and active waveform synthesis can be used as complementary tools to protect coherence while recovering controllability. This strategy is not tied to a specific filter implementation, but can be adapted to different qubit frequencies, device parameters, and line responses. A natural next step is the extension to multiplexed and multi-qubit fluxonium processors. There, the same framework could support shared-line operation through carrier multiplexing and instruction-level waveform synthesis. While larger systems will impose tighter requirements on spectral isolation, cross-talk suppression, and calibration stability, our results suggest that simplified wiring can remain compatible with high-fidelity control.

VI. DATA AVAILABILITY STATEMENT

The data that support the findings of this study are available from the corresponding author upon reasonable request.

ACKNOWLEDGMENTS

This research was supported by the Guangdong Provincial Quantum Science Strategic Initiative (Grant No. GDZX2407001). The authors express their gratitude to the Westlake Center for Micro/Nano Fabrication, Zhejiang QizhenTek Co., Ltd., and the Micro-Nano Fabrication and Device Center at the Songshan Lake Materials Laboratory for their essential technical support during the chip fabrication process.

Appendix A: Flux line setup

We decompose the external magnetic flux into a static bias and a small time-dependent component,

$$\Phi(t) = \Phi_{\rm dc} + \delta\Phi(t). \tag{A1}$$

The static flux bias sets the operating point of the qubit and is incorporated into the Josephson term. Applying a phase-translation operator, the fluxonium Hamiltonian is then written as

$$H_0 = 4E_C\hat{n}^2 + \frac{1}{2}E_L\hat{\phi}^2 - E_J\cos(\hat{\phi} - \phi_{\rm dc}), \tag{A2}$$

where $\phi_{\rm dc} = 2\pi\Phi_{\rm dc}/\Phi_0$. The time-dependent flux $\delta\Phi(t)$ is coupled inductively through the superinductor. Introducing the reduced flux

$$\delta\phi(t) = 2\pi\frac{\delta\Phi(t)}{\Phi_0}, \tag{A3}$$

the inductive term becomes

$$\frac{1}{2}E_L\left(\hat{\phi} - \delta\phi(t)\right)^2. \tag{A4}$$

Expanding to first order in $\delta\phi(t)$, we obtain

$$\frac{1}{2}E_L\left(\hat{\phi} - \delta\phi(t)\right)^2 = \frac{1}{2}E_L\hat{\phi}^2 - E_L\hat{\phi}\,\delta\phi(t) + \mathcal{O}(\delta\phi^2). \tag{A5}$$

The linear term defines the drive Hamiltonian,

$$\Delta H(t) = -E_L\hat{\phi}\,\delta\phi(t). \tag{A6}$$

The flux modulation is generated by a drive current $I_d(t)$ through a mutual inductance M, leading to

$$\delta\phi(t) = 2\pi \frac{M I_d(t)}{\Phi_0}. \tag{A7}$$

Substituting this into the drive Hamiltonian yields

$$\Delta H(t) = -E_L \cdot 2\pi \frac{M I_d(t)}{\Phi_0}\,\hat{\phi}. \tag{A8}$$

1. Rabi Drive Strength from Room-Temperature Voltage

To connect the drive Hamiltonian to the room-temperature control electronics, we express the drive current $I_d(t)$ in terms of the voltage generated by the arbitrary waveform generator (AWG). Let $V_{\rm awg}(t)$ be the room-temperature voltage signal. The control line includes a series of attenuators with a total voltage attenuation factor α (where $\alpha < 1$) and a characteristic line impedance Z_0 (typically 50 Ω). The effective current reaching the flux bias line at the base temperature is

$$I_d(t) = \frac{\alpha V_{\rm awg}(t)}{Z_0}. \tag{A9}$$

Substituting this into the drive Hamiltonian, we obtain

$$\Delta H(t) = -\left(2\pi E_L \frac{M}{\Phi_0}\frac{\alpha}{Z_0}\right) V_{\rm awg}(t)\,\hat{\phi}. \tag{A10}$$

For a resonant AC drive $V_{\rm awg}(t) = V_0\cos(\omega_d t)$, where ω_d is close to the qubit transition frequency ω_{ge} between the ground state $|0\rangle$ and the first excited state $|1\rangle$, we can apply the rotating-wave approximation (RWA). The effective drive strength, defined as the Rabi frequency Ω_R, is determined by the transition matrix element of the phase operator $\langle 0|\hat{\phi}|1\rangle$:

$$\hbar\Omega_R = \left|2\pi E_L \frac{M}{\Phi_0}\frac{\alpha}{Z_0}\right| V_0\,|\langle 0|\hat{\phi}|1\rangle|. \tag{A11}$$

This equation directly relates the room-temperature drive amplitude V_0 to the resulting Rabi frequency, providing a deterministic calibration for the transverse control.

2. Relaxation Time Degradation Induced by Room-Temperature White Noise

In addition to the coherent drive, the physical connection to room-temperature electronics introduces wideband noise, which can stimulate spurious transitions and degrade the qubit relaxation time T_1. The noise current on the flux line is characterized by its quantum noise spectral density $S_{II}(\omega)$. According to Fermi's Golden Rule, the transition rate from $|1\rangle$ to $|0\rangle$ induced by the flux line noise is given by

$$\Gamma^{\rm line}_{1\to 0} = \frac{1}{\hbar^2}\left(2\pi E_L \frac{M}{\Phi_0}\right)^2 |\langle 0|\hat{\phi}|1\rangle|^2 S_{II}(\omega_{ge}). \tag{A12}$$

Assuming the dominant noise source originates from the room-temperature electronics (e.g., AWG voltage white noise or thermal noise at 300 K) that propagates down the control line, the effective voltage noise spectral density at the AWG output is denoted as $S^{\rm awg}_{VV}(\omega)$. After passing through the attenuation chain, the current noise spectral density at the qubit plane becomes

$$S_{II}(\omega_{ge}) = \frac{\alpha^2}{Z_0^2} S^{\rm awg}_{VV}(\omega_{ge}). \tag{A13}$$

Substituting the current noise spectral density into the transition rate, the noise-induced relaxation rate $\Gamma^{\rm line}_{1\to 0} = 1/T_1^{\rm line}$ is

$$\frac{1}{T_1^{\rm line}} = \frac{1}{\hbar^2}\left(2\pi E_L \frac{M}{\Phi_0}\frac{\alpha}{Z_0}\right)^2 |\langle 0|\hat{\phi}|1\rangle|^2 S^{\rm awg}_{VV}(\omega_{ge}). \tag{A14}$$

This result highlights a fundamental physical trade-off in the unified control architecture: while increasing the effective coupling (by increasing M or decreasing the attenuation α) enhances the Rabi frequency Ω_R for faster gate operations, it simultaneously quadratically increases the qubit's susceptibility to room-temperature wideband noise, thereby suppressing the T_1 limit. This strictly necessitates the deployment of frequency-selective filtering to suppress $S^{\rm awg}_{VV}(\omega_{ge})$ while maintaining high transparency at low frequencies. To evaluate the specific impact of room-temperature electronics, we model the wideband fluctuations as frequency-independent white noise. The effective voltage noise spectral density $S^{\rm awg}_{VV}(\omega)$ at the input of the control line is typically dominated by two sources: the Johnson–Nyquist thermal noise at room temperature ($T_{\rm rt} = 300$ K) and the intrinsic noise floor of the AWG. The double-sided thermal noise spectral density is given by

$$S^{\rm th}_{VV}(\omega) = 2k_B T_{\rm rt} Z_0, \tag{A15}$$

where k_B is the Boltzmann constant. In practical experimental setups, the active noise floor of the AWG is often significantly higher than the 300 K thermal background. If the AWG exhibits a constant white noise power spectral density $P_{\rm noise}$ (in W/Hz), the corresponding double-sided voltage noise spectral density becomes

$$S^{\rm awg}_{VV}(\omega) = \frac{1}{2} P_{\rm noise} Z_0. \tag{A16}$$

Substituting this effective $S^{\rm awg}_{VV}(\omega_{ge})$ back into the transition rate equation allows us to quantitatively predict the Purcell-like T_1 degradation induced by the specific unified-drive electronics. It is important to note that in our main text analysis, we exclusively consider the input noise from the AWG, as the technical noise floor of the room-temperature electronics overwhelmingly dominates the standard Johnson-Nyquist thermal noise.

Appendix B: Experimental Setup

The cryogenic wiring is detailed in Fig. 4. The device is mounted at the 15 mK base stage of a dilution refrigerator, enclosed within multiple layers of magnetic and infrared (IR) shielding. The setup consists of standard readout input/output lines and two flux lines: a unified dynamic control line and a static DC-flux line. The readout input line is thermalized with 80 dB of distributed attenuation, while the output line features cascaded isolators and a high-electron-mobility transistor (HEMT) amplifier at 4 K to optimize the signal-to-noise ratio and protect the qubit from back-action.

The unified dynamic control line mediates both the transverse microwave drive (XY control) and the dynamic longitudinal tuning (Z control). To balance drive strength and coherence, this line is equipped with 30 dB of cryogenic attenuation. Crucially, a Gaussian low-pass filter with a 92 MHz 3-dB cutoff is installed at the 4 K stage to strictly suppress wideband noise near the qubit transition frequency.The static DC-flux line is heavily low-pass filtered to set the baseline operating point (e.g., the half-flux sweet spot). The dynamic and static flux signals are subsequently combined via a cryogenic bias-tee at the base stage before coupling to the qubit. Notably, this dedicated DC-flux line is used here for experimental convenience; in future scaled-up architectures, it can be entirely replaced by a global magnetic field bias, leaving the unified dynamic line as the sole local routing overhead per qubit.

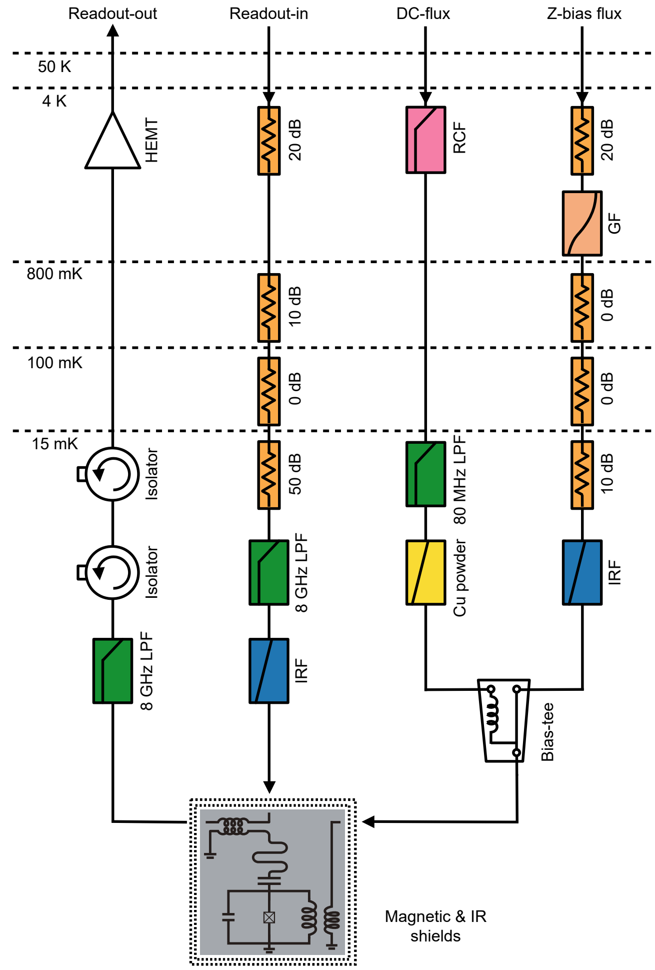

FIG. 4. **Cryogenic Setup.** Schematic detailing the low-temperature wiring inside the dilution refrigerator for unified control.

Appendix C: Coherence Analysis

To characterize the decoherence mechanisms of the unified single-port architecture, we measure the energy relaxation time T_1 and the pure dephasing time T_ϕ of the fluxonium qubit as a function of the external magnetic flux $\Phi_{\rm ext}$. During these measurements, the qubit is idled at various flux biases using the dynamic Z-control channel, while all microwave excitation and readout operations are performed at the half-flux sweet spot ($\Phi_{\rm ext} = 0.5\Phi_0$).

For each flux bias $\Phi_{\rm ext}$, the measured excited-state population $P_e(t)$ is first fitted using a double-exponential relaxation model. This model accounts for deviations from a simple single-exponential decay, which can arise from quasiparticle-related relaxation dynamics [39, 40]. The fitted population decay is described by

$$P_e(t) = A\exp(-t/T_{\rm exp})\exp\{n_{\rm qp}[\exp(-t/T_{\rm qp}) - 1]\} + B, \tag{C1}$$

where $T_{\rm exp}$ and $T_{\rm qp}$ are characteristic relaxation times, $n_{\rm qp}$ is the quasiparticle density parameter, A is the initial amplitude, and B accounts for the measurement baseline. Because the decay is non-exponential, we do not report a single fitted rate parameter. Instead, we define an effective relaxation time T_1 as the time at which the fitted relaxation curve reaches the $1/e$ population level relative to its initial amplitude. This approach provides a consistent metric for energy relaxation across the entire flux tuning range.

To extract the pure dephasing time T_ϕ, we perform Ramsey, Hahn echo, and Carr-Purcell-Meiboom-Gill (CPMG) measurements. The envelope of the state projection signal $P_{env}(t)$ in these transverse relaxation measurements is fitted to a mixed exponential-plus-Gaussian decay function [27, 41, 42]:

$$P_{env}(t) = C\exp\left(-\frac{t}{2T_1^{\rm DE}}\right)\exp\left[-\frac{t}{T_{\phi,\rm exp}} - \left(\frac{t}{T_{\phi,\rm G}}\right)^2\right] + D. \tag{C2}$$

Here, the term $\exp[-t/(2T_1^{\rm DE})]$ represents the fixed relaxation contribution, where $T_1^{\rm DE}$ denotes the relaxation time scale derived directly from the double-exponential (DE) fit to the T_1 data, rather than the effective $1/e$ time. The pure dephasing is then characterized by both an exponential time constant $T_{\phi,\rm exp}$ and a Gaussian time constant $T_{\phi,\rm G}$. Away from the sweet spot, low-frequency

$1/f$ flux noise becomes the dominant dephasing channel, which manifests as a Gaussian decay profile. Therefore, in our analysis, we extract the Gaussian component $T_\phi \equiv T_{\phi,\mathrm{G}}$ as the relevant pure-dephasing time.

As shown in Fig. 5(a), the effective energy relaxation time T_1 is generally maintained between 100 and 200 μs near the half-flux sweet spot. When the flux is tuned away from this optimal point, T_1 exhibits noticeable fluctuations and several sharp, precipitous drops (e.g., near $\Phi_{\mathrm{ext}}/\Phi_0 \approx 0.55$). These narrow-band suppressions of the relaxation time are characteristic signatures of resonant interactions with randomly distributed two-level system (TLS) defects in the device environment [3, 25, 43, 44].

The flux dependence of the extracted pure dephasing time T_ϕ is presented in Fig. 5(b). At the half-flux sweet spot ($\Phi_{\mathrm{ext}} = 0.5\Phi_0$), the qubit transition frequency is first-order insensitive to flux variations ($d\omega_{ge}/d\Phi_{\mathrm{ext}} = 0$), leading to a strongly peaked T_ϕ that exceeds 100 μs. As the flux bias moves away from the sweet spot, the qubit frequency becomes highly sensitive to local magnetic flux fluctuations, causing T_ϕ to drop rapidly to the single-microsecond regime. This steep decline is primarily driven by the aforementioned low-frequency $1/f$ flux noise [45, 46]. By employing dynamical decoupling techniques, the low-frequency phase accumulation can be effectively mitigated. As shown in Fig. 5(b), increasing the number of refocusing π pulses in the CPMG(N) sequences progressively filters out the low-frequency noise components, significantly extending T_ϕ away from the sweet spot.

To further identify the physical origins of decoherence, we perform independent fits to the flux-dependent T_1 and T_ϕ data using a comprehensive noise model. The resulting fit curves are shown as solid lines in Fig. 5. We first fit the pure dephasing data to a model dominated by low-frequency $1/f$ flux noise and a frequency-independent white noise floor, yielding a $1/f$ flux noise amplitude of $A_\Phi \approx 8.11 \pm 0.09\ \mu\Phi_0$ and a white flux noise amplitude of $A_w \approx 4.18 \pm 0.27\ n\Phi_0/\sqrt{\mathrm{Hz}}$. Using the extracted $1/f$ flux noise intensity as a fixed parameter, we then fit the relaxation data to a model incorporating dielectric loss from TLS, $1/f$ flux noise, and an additional free static noise term. This procedure yields an effective dielectric loss tangent of $\tan\delta_C \approx 13.7 \times 10^{-6}$. These quantitative results confirm that the qubit coherence is governed by the interplay between TLS-induced dielectric loss and magnetic flux fluctuations.

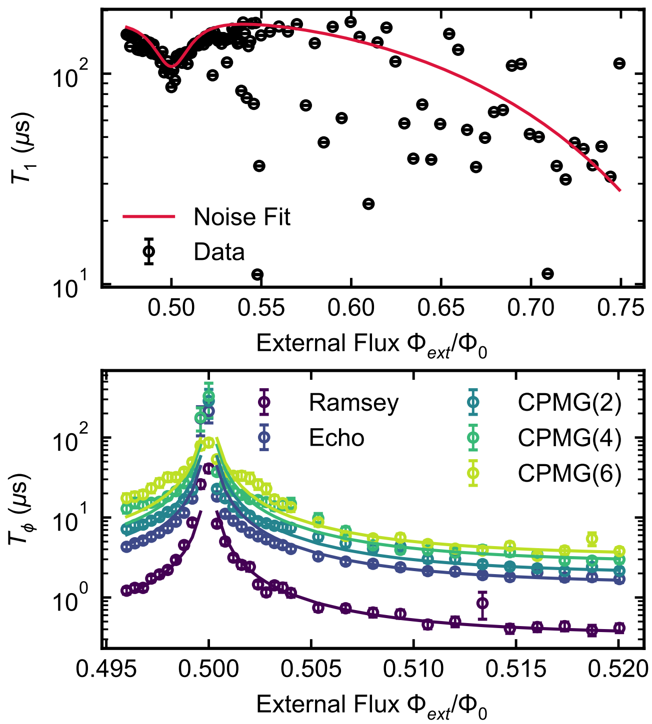

FIG. 5. **Coherence vs. Flux.** (a) Energy relaxation time T_1 as a function of the external flux. (b) Pure dephasing time T_ϕ extracted from Ramsey, Hahn echo, and CPMG sequences with varying numbers of refocusing π pulses as a function of the external flux.

Appendix D: Summary of All Tested Devices

The same approach has also been tested on multiple additional devices, as summarized in Table I. Device A corresponds to the qubit discussed in the main text. Devices B, C, D, and E all support high-fidelity control, with extracted single-qubit gate fidelities above 99.97%. Devices F and G were not fully benchmarked by randomized benchmarking, but both support standard gate operations and exhibit coherence times with $T_1 > 100\ \mu$s. Device H, with a substantially higher qubit frequency, can still be operated under the same control architecture, but the 92 MHz low-pass filter requires significantly longer pulses, with gate durations extended to about 200 ns. Taken together, these results indicate that a single 92 MHz low-pass filter is sufficient to support high-fidelity control for fluxonium qubits with transition frequencies below approximately 300 MHz.

More broadly, these results clarify both the applicability and the limitation of the present design. For qubits in the sub-300 MHz range, strong low-pass filtering can simultaneously preserve long coherence and support accurate compensated control. At higher qubit frequencies, the same filtering strategy remains conceptually valid, but maintaining short and high-fidelity gates requires correspondingly larger filter bandwidth. This does not alter the main conclusion of this work. Rather, it reinforces the central design principle: unified single-port control is enabled not by a specific cutoff frequency, but by the joint use of frequency-selective filtering and waveform compensation.

TABLE I. Results of all tested devices.

Device	f_q(MHz)	Fidelity (%)	T_g (ns)	$T_1(\mu s)$	$T_2^R(\mu s)$	$T_2^{\text{echo}}(\mu s)$
A	208	99.990	20	110	128	133
B	205	99.974	20	65	21	34
C	232	99.986	20	95	82	118
D	285	99.970	40	53	30	34
E	267	99.974	30	52	23	46
F	233	N/A	20	140	28	28
G	164	N/A	20	151	30	79
H	378	N/A	200	214	68	131

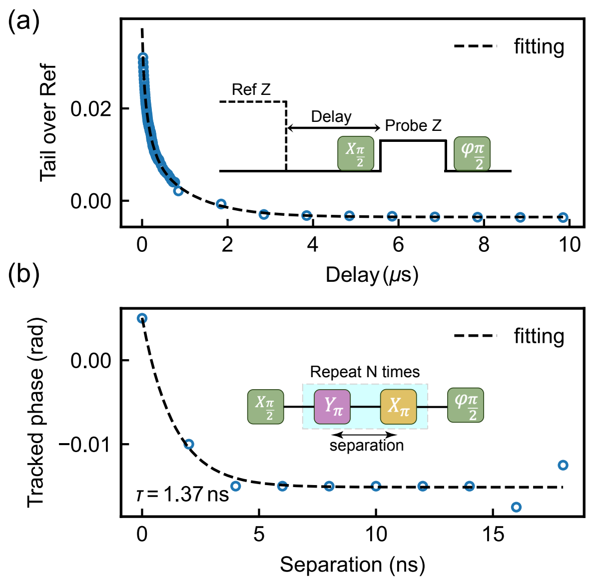

FIG. 6. **Distortion Characterization in the Unified Single-port Architecture.** (a) Long-tail response of the Z control channel, measured by converting the phase accumulated during a delayed probe window into the equivalent normalized residual Z-pulse tail. The dashed line is an exponential fit used for IIR-based compensation. (b) Assessment of residual microwave intra-quadrature distortion using alternating Y_π and X_π pulses. The dashed line is a single-exponential fit with a characteristic decay time of 1.37 ns, indicating that the residual tail is sufficiently short that no further correction is applied.

Appendix E: Distortion characterization

To assess the dominant waveform imperfections in the unified single-port architecture, we separately characterize the settling dynamics of the low-frequency Z channel and the residual temporal distortion in the microwave control channel. The corresponding measurements are summarized in Fig. 6. For the Z channel, the dominant imperfection is a long-tail response following the falling edge of a nominally rectangular flux pulse. Such settling behavior may arise from impedance mismatch, surface-related relaxation, or effective LR-type filtering in the flux-control path, and it can introduce unwanted phase accumulation in subsequent qubit operations. To quantify this effect, we use the qubit as an in-situ detector. As shown in Fig. 6(a), a long reference Z pulse is first applied to generate a well-defined falling edge. After a variable delay, a short probe pulse shifts the qubit to a flux-sensitive point, where the residual tail accumulated during the probe window is converted into a measurable phase shift through a Ramsey-type sequence [25]. In the present analysis, rather than deconvolving the full flux-distortion waveform from the measured phase, we directly convert the phase into the equivalent residual Z-pulse tail normalized to the reference-pulse amplitude. The vertical axis in Fig. 6(a) therefore directly represents the relative settling tail, denoted as "Tail over Ref".

The extracted Z-pulse tail is well described by a multi-exponential relaxation model. From the fit, we obtain three settling times of approximately 34 ns, 170 ns, and 996 ns, with corresponding normalized amplitudes of -1.74%, -1.89%, and -1.58%, respectively. These results indicate that the Z-line distortion contains both intermediate and long-timescale components, consistent with slow settling processes in the flux-control path. The extracted parameters provide a compact description of the low-frequency response and directly motivate the use of IIR-based compensation for the Z channel.

Microwave pulse distortions can in general be divided into intra-quadrature distortion and cross-quadrature distortion. For an ideal resonant drive, the effective Hamiltonian in the rotating frame is

$$H_{\text{ideal}}(t) = \frac{\Omega(t)}{2}\sigma_x, \tag{E1}$$

where $\Omega(t)$ is the target pulse envelope. Intra-quadrature distortion corresponds to residual errors that remain in the same quadrature channel, leading to

$$H_{\text{intra}}(t) = \frac{\Omega(t) + \delta\Omega_x(t)}{2}\sigma_x, \tag{E2}$$

which mainly gives rise to coherent over- or under-rotation without changing the nominal rotation axis. By contrast, cross-quadrature distortion introduces an orthogonal component,

$$H_{\text{cross}}(t) = \frac{\Omega(t)}{2}\sigma_x + \frac{\delta\Omega_y(t)}{2}\sigma_y, \tag{E3}$$

thereby tilting the effective rotation axis in the rotating frame.

In our experiment, qubit control is implemented using direct microwave flux drive. The flux-drive operator predominantly couples the $|g\rangle \leftrightarrow |e\rangle$ transition, while its coupling to higher transitions is strongly suppressed. As a result, temporal waveform imperfections are expected to remain predominantly within the effective control quadrature. Nevertheless, a residual tail left by a preceding pulse can still appear as a small orthogonal correction during the following operation and therefore can be detected through its induced phase shift.

To characterize this effect, we employ alternating Y_π and X_π pulses, as shown in Fig. 6(b). Physically, a distorted Y_π pulse leaves a weak temporal tail that persists into the subsequent X_π pulse. The effective Hamiltonian during the X_π operation can therefore be written as

$$H_{\text{eff}} = \frac{\Omega_x(t)}{2}\sigma_x + \frac{\delta\Omega_y(t-t_d)}{2}\sigma_y, \tag{E4}$$

where t_d is the delay between neighboring pulses. The residual tail tilts the effective rotation axis and produces a small coherent phase shift,

$$\phi_s \approx \frac{\delta\Omega_y}{\Omega_x}. \tag{E5}$$

This phase accumulation can be measured in a Ramsey-type interference experiment by scanning both the pulse separation and the phase of the final analysis pulse.

As shown in Fig. 6(b), the measured phase is well described by a single-exponential decay with a characteristic time of only 1.37 ns. This timescale is much shorter than the gate duration relevant for the present experiment, indicating that the residual microwave tail is already weak and rapidly decaying. Accordingly, we do not apply any further correction based on this measurement. Instead, this experiment serves only as an assessment of the residual microwave distortion level, rather than as an input for determining the FIR coefficients. Taken together with the Z-channel measurement, these results indicate that the dominant correctable settling error in our setup arises from the low-frequency flux path, while the residual microwave tail is sufficiently short that no additional correction is required.

Appendix F: FIR coefficient synthesis for microwave compensation

The FPGA FIR coefficients are synthesized directly from the compensated transfer function $H_{\text{inv}}(f)$ obtained in the main text. First, the target gain profile is sampled on a dense frequency grid from dc to the Nyquist frequency,

$$G(f) = |H_{\text{inv}}(f)|. \tag{F1}$$

The sampled frequency response is then used as the design target for a 16-tap linear-phase FIR filter using frequency-domain synthesis. Since an even number of symmetric taps is adopted, the filter belongs to the Type-II FIR class, whose response is constrained to vanish at the Nyquist frequency. Accordingly, the target gain at the Nyquist frequency is explicitly set to zero before the synthesis procedure.

After obtaining the floating-point FIR coefficients h_i, the coefficients are normalized to the maximum absolute value and quantized into signed 16-bit integers for FPGA implementation,

$$h_i^{(\text{int16})} = \text{round}\left(\frac{h_i}{\max|h_i|} \times 32767\right). \tag{F2}$$

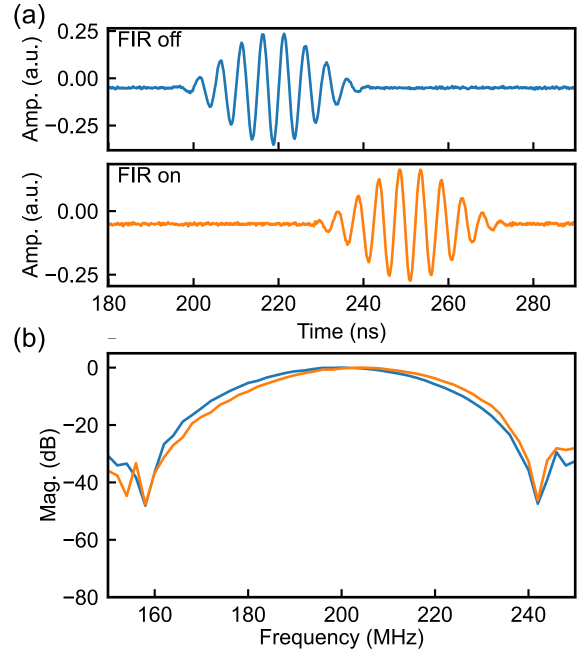

FIG. 7. **FIR Coefficient Synthesis and Measured Waveform Reshaping.** (a) Measured output waveforms with the FIR block disabled (top) and enabled (bottom). The 16-tap FIR coefficients are generated from the target bounded inverse transfer function by frequency-domain sampling, linear-phase filter synthesis, and 16-bit quantization for FPGA implementation. With FIR enabled, the waveform is visibly reshaped and shifted in time, reflecting the causal group delay and spectral reweighting introduced by the digital filter. (b) Measured spectra of the corresponding waveforms with FIR off (blue) and FIR on (orange). The FIR-on waveform exhibits reduced low-frequency spectral weight and enhanced higher-frequency components around the qubit control band, consistent with the intended pre-compensation of the downstream low-pass response.

The final FIR coefficients used in the experiment are $h_{\text{FIR}} = [-300,\ 145,\ 977,\ 3351,\ -682,\ -9355,\ -25925,\ 32767,\ 32766,\ -25925,\ -9355,\ -682,\ 3351,\ 977,\ 145,\ -300]$.

The effect of this digital filter is shown in Fig. 7. In the time domain, enabling the FIR block visibly reshapes the output waveform and introduces a temporal shift relative to the FIR-off case. This shift is the expected consequence of causal digital filtering and reflects the finite group delay of the FIR process. At the same time, the envelope is redistributed in a way consistent with pre-compensation. In the frequency domain, the FIR-on waveform exhibits suppressed low-frequency spectral weight and relatively enhanced higher-frequency components around the qubit control band. This spectral redistribution is precisely the intended function of the digital compensation: rather than simply amplifying the entire waveform, the FIR selectively suppresses the slowly varying part of the signal while boosting the faster components needed to counteract the downstream low-pass response. In this way, the FIR block provides a hardware-compatible implementation of the compensated microwave waveform synthesis discussed in the main text.

[1] A. P. Place, L. V. Rodgers, P. Mundada, B. M. Smitham, M. Fitzpatrick, Z. Leng, A. Premkumar, J. Bryon, A. Vrajitoarea, S. Sussman, *et al.*, Nat. Commun. **12**, 1779 (2021).

[2] S. Ganjam, Y. Wang, Y. Lu, A. Banerjee, C. U. Lei, L. Krayzman, K. Kisslinger, C. Zhou, R. Li, Y. Jia, *et al.*, Nat. Commun. **15**, 3687 (2024).

[3] L. B. Nguyen, Y.-H. Lin, A. Somoroff, R. Mencia, N. Grabon, and V. E. Manucharyan, Phys. Rev. X **9**, 041041 (2019).

[4] A. Somoroff, Q. Ficheux, R. A. Mencia, H. Xiong, R. Kuzmin, and V. E. Manucharyan, Phys. Rev. Lett. **130**, 267001 (2023).

[5] F. Wang, K. Lu, H. Zhan, L. Ma, F. Wu, H. Sun, H. Deng, Y. Bai, F. Bao, X. Chang, R. Gao, X. Gao, G. Gong, L. Hu, R. Hu, H. Ji, X. Ma, L. Mao, Z. Song, C. Tang, *et al.*, Phys. Rev. Appl. **23**, 044064 (2025).

[6] Y. Sung, L. Ding, J. Braumüller, A. Vepsäläinen, B. Kannan, M. Kjaergaard, A. Greene, G. O. Samach, C. McNally, D. Kim, *et al.*, Phys. Rev. X **11**, 021058 (2021).

[7] V. Negîrneac, H. Ali, N. Muthusubramanian, F. Battistel, R. Sagastizabal, M. S. Moreira, J. F. Marques, W. J. Vlothuizen, M. Beekman, C. Zachariadis, N. Haider, A. Bruno, and L. DiCarlo, Phys. Rev. Lett. **126**, 220502 (2021).

[8] L. Ding, M. Hays, Y. Sung, B. Kannan, J. An, A. Di Paolo, A. H. Karamlou, T. M. Hazard, K. Azar, D. K. Kim, B. M. Niedzielski, A. Melville, M. E. Schwartz, J. L. Yoder, T. P. Orlando, S. Gustavsson, J. A. Grover, K. Serniak, and W. D. Oliver, Phys. Rev. X **13**, 031035 (2023).

[9] D. A. Rower, L. Ding, H. Zhang, M. Hays, J. An, P. M. Harrington, I. T. Rosen, J. M. Gertler, T. M. Hazard, B. M. Niedzielski, *et al.*, PRX Quantum **5**, 040342 (2024).

[10] Z. Zhan, Z. Li, F. Wang, W. Lan, X. Pan, L. Xiang, X. Dou, R. Gao, G. Gong, Y. Guo, *et al.*, arXiv preprint arXiv:2604.13363 (2026), arXiv:2604.13363.

[11] F. Arute, K. Arya, R. Babbush, D. Bacon, J. C. Bardin, R. Barends, R. Biswas, S. Boixo, F. G. Brandao, D. A. Buell, *et al.*, Nature **574**, 505 (2019).

[12] Y. Wu, W.-S. Bao, S. Cao, F. Chen, M.-C. Chen, X. Chen, T.-H. Chung, H. Deng, Y. Du, D. Fan, M. Gong, C. Guo, C. Guo, S. Guo, L. Han, L. Hong, H.-L. Huang, Y.-H. Huo, L. Li, N. Li, *et al.*, Phys. Rev. Lett. **127**, 180501 (2021).

[13] Y. Kim, A. Eddins, S. Anand, K. X. Wei, E. Van Den Berg, S. Rosenblatt, H. Nayfeh, Y. Wu, M. Zaletel, K. Temme, *et al.*, Nature **618**, 500 (2023).

[14] J. Van Damme, S. Massar, R. Acharya, T. Ivanov, D. Perez Lozano, Y. Canvel, M. Demarets, D. Vangoidsenhoven, Y. Hermans, J. Lai, *et al.*, Nature **634**, 74 (2024).

[15] F. Jin, S. Jiang, X. Zhu, Z. Bao, F. Shen, K. Wang, Z. Zhu, S. Xu, Z. Song, J. Chen, Z. Tan, Y. Wu, C. Zhang, Y. Gao, N. Wang, Y. Zou, A. Zhang, T. Li, J. Zhong, Z. Cui, *et al.*, Nature **645**, 626 (2025).

[16] J. Koch, T. M. Yu, J. Gambetta, A. A. Houck, D. I. Schuster, J. Majer, A. Blais, M. H. Devoret, S. M. Girvin, and R. J. Schoelkopf, Phys. Rev. A **76**, 042319 (2007).

[17] V. E. Manucharyan, J. Koch, L. I. Glazman, and M. H. Devoret, Science **326**, 113 (2009).

[18] P. Krantz, M. Kjaergaard, F. Yan, T. P. Orlando, S. Gustavsson, and W. D. Oliver, Appl. Phys. Rev. **6**, 10.1063/1.5089550 (2019).

[19] R. Manenti, E. A. Sete, A. Q. Chen, S. Kulshreshtha, J.-H. Yeh, F. Oruc, A. Bestwick, M. Field, K. Jackson, and S. Poletto, Appl. Phys. Lett. **119**, 10.1063/5.0065517 (2021).

[20] Z. Yan, Z.-Y. Ge, R. Li, Y.-R. Zhang, F. Nori, and Y. Nakamura, Sci. Adv. **12**, eaeb8213 (2026).

[21] H. Zhang, S. Chakram, T. Roy, N. Earnest, Y. Lu, Z. Huang, D. K. Weiss, J. Koch, and D. I. Schuster, Phys. Rev. X **11**, 011010 (2021).

[22] C. Deng, J.-L. Orgiazzi, F. Shen, S. Ashhab, and A. Lupascu, Phys. Rev. Lett. **115**, 133601 (2015).

[23] X. Ma, G. Zhang, F. Wu, F. Bao, X. Chang, J. Chen, H. Deng, R. Gao, X. Gao, L. Hu, H. Ji, H.-S. Ku, K. Lu, L. Ma, L. Mao, Z. Song, H. Sun, C. Tang, F. Wang, H. Wang, *et al.*, Phys. Rev. Lett. **132**, 060602 (2024).

[24] Q. Ficheux, L. B. Nguyen, A. Somoroff, H. Xiong, K. N. Nesterov, M. G. Vavilov, and V. E. Manucharyan, Phys. Rev. X **11**, 021026 (2021).

[25] F. Bao, H. Deng, D. Ding, R. Gao, X. Gao, C. Huang, X. Jiang, H.-S. Ku, Z. Li, X. Ma, X. Ni, J. Qin, Z. Song, H. Sun, C. Tang, T. Wang, F. Wu, T. Xia, W. Yu, F. Zhang, *et al.*, Phys. Rev. Lett. **129**, 010502 (2022).

[26] C. Huang, T. Wang, F. Wu, D. Ding, Q. Ye, L. Kong, F. Zhang, X. Ni, Z. Song, Y. Shi, H.-H. Zhao, C. Deng, and J. Chen, Phys. Rev. Lett. **130**, 070601 (2023).

[27] T. Wang, F. Wu, F. Wang, X. Ma, G. Zhang, J. Chen, H. Deng, R. Gao, R. Hu, L. Ma, *et al.*, Phys. Rev. Lett. **132**, 230601 (2024).

[28] M. McEwen, D. Kafri, Z. Chen, J. Atalaya, K. Satzinger, C. Quintana, P. V. Klimov, D. Sank, C. Gidney, A. Fowler, *et al.*, Nat. Commun. **12**, 1761 (2021).

[29] M. D. Reed, B. R. Johnson, A. A. Houck, L. DiCarlo, J. M. Chow, D. I. Schuster, L. Frunzio, and R. J. Schoelkopf, Appl. Phys. Lett. **96**, 203110 (2010).

[30] S. Krinner, S. Storz, P. Kurpiers, P. Magnard, J. Heinsoo, R. Keller, J. Luetolf, C. Eichler, and A. Wallraff, EPJ Quantum Technol. **6**, 2 (2019).

[31] S. Simbierowicz, M. Borrelli, V. Monarkha, V. Nuutinen, and R. E. Lake, PRX Quantum **5**, 030302 (2024).

[32] M. Xia, C. Zhou, C. Liu, P. Patel, X. Cao, P. Lu, B. Mesits, M. Mucci, D. Gorski, D. Pekker, *et al.*, Nat. Commun. 10.1038/s41467-025-67766-6 (2025).

[33] J. Schirk, F. Wallner, L. Huang, I. Tsitsilin, N. Bruckmoser, L. Koch, D. Bunch, N. J. Glaser, G. B. Huber, M. Knudsen, *et al.*, PRX Quantum **6**, 030315 (2025).

[34] X. You, J. A. Sauls, and J. Koch, Phys. Rev. B **99**, 174512 (2019).

[35] E. A. Sete, J. M. Gambetta, and A. N. Korotkov, Phys.

Rev. B **89**, 104516 (2014).
[36] E. Magesan, J. M. Gambetta, B. R. Johnson, C. A. Ryan, J. M. Chow, S. T. Merkel, M. P. Da Silva, G. A. Keefe, M. B. Rothwell, T. A. Ohki, *et al.*, Phys. Rev. Lett. **109**, 080505 (2012).
[37] Y. Yang, Z. Shen, X. Zhu, Z. Wang, G. Zhang, J. Zhou, X. Jiang, C. Deng, and S. Liu, Rev. Sci. Instrum. **93**, 10.1063/5.0085467 (2022).
[38] M. A. Rol, L. Ciorciaro, F. K. Malinowski, B. M. Tarasinski, R. E. Sagastizabal, C. C. Bultink, Y. Salathe, N. Haandbæk, J. Sedivy, and L. DiCarlo, Appl. Phys. Lett. **116**, 10.1063/1.5133894 (2020).
[39] I. M. Pop, K. Geerlings, G. Catelani, R. J. Schoelkopf, L. I. Glazman, and M. H. Devoret, Nature **508**, 369 (2014).
[40] K. Serniak, M. Hays, G. de Lange, S. Diamond, S. Shankar, L. D. Burkhart, L. Frunzio, M. Houzet, and M. H. Devoret, Phys. Rev. Lett. **121**, 157701 (2018).
[41] G. Ithier, E. Collin, P. Joyez, P. J. Meeson, D. Vion, D. Esteve, F. Chiarello, A. Shnirman, Y. Makhlin, J. Schriefl, and G. Schön, Phys. Rev. B **72**, 134519 (2005).
[42] J. Bylander, S. Gustavsson, F. Yan, F. Yoshihara, K. Harrabi, G. Fitch, D. G. Cory, Y. Nakamura, J.-S. Tsai, and W. D. Oliver, Nat. Phys. **7**, 565 (2011).
[43] J. M. Martinis, K. B. Cooper, R. McDermott, M. Steffen, M. Ansmann, K. D. Osborn, K. Cicak, S. Oh, D. P. Pappas, R. W. Simmonds, and C. C. Yu, Phys. Rev. Lett. **95**, 210503 (2005).
[44] C. Müller, J. H. Cole, and J. Lisenfeld, Rep. Prog. Phys. **82**, 124501 (2019).
[45] F. Yoshihara, K. Harrabi, A. O. Niskanen, Y. Nakamura, and J. S. Tsai, Phys. Rev. Lett. **97**, 167001 (2006).
[46] E. Paladino, Y. M. Galperin, G. Falci, and B. L. Altshuler, Rev. Mod. Phys. **86**, 361 (2014).